IOP Publishing
Plasma Sources Science and Technology
Plasma Sources Sci. Technol. **31** (2022) 055017 (13pp)
https://doi.org/10.1088/1361-6595/ac6e05

Control of ion flux-energy distributions by low frequency square-shaped tailored voltage waveforms in capacitively coupled plasmas

P Hartmann[1], I Korolov[2], J Escandón-López[3], W van Gennip[3], K Buskes[3] and J Schulze[2,4,*]

[1] Institute for Solid State Physics and Optics, Wigner Research Centre for Physics, H-1121 Budapest, Konkoly-Thege Miklós str. 29-33, Hungary
[2] Department of Electrical Engineering and Information Science, Ruhr-University Bochum, D-44780 Bochum, Germany
[3] Prodrive Technologies B.V., Science Park Eindhoven 5006, 5692 EL Son, The Netherlands
[4] Key Laboratory of Materials Modification by Laser, Ion, and Electron Beams (Ministry of Education), School of Physics, Dalian University of Technology, Dalian 116024, People's Republic of China

E-mail: schulze@aept.ruhr-uni-bochum.de

Received 8 January 2022, revised 20 April 2022
Accepted for publication 9 May 2022
Published 31 May 2022

Abstract

Capacitively coupled plasmas are routinely used in an increasing number of technological applications, where a precise control of the quantity and the shape of the energy distribution of ion fluxes impacting boundary surfaces is required. Oftentimes, narrow peaks at controllable energies are required, e.g. to improve selectivity in plasma etching, which cannot be realized in classical discharges. We combine experimental ion flux-energy distribution measurements and PIC/MCC simulations to provide insights into the operation and ion acceleration mechanisms for discharges driven by square-shaped tailored voltage waveforms composed of low-frequency (100 kHz) pulsed and high-frequency (27.12 MHz) signals. The formation of ion flux-energy distributions with a narrow high energy peak and strongly reduced ion fluxes at intermediate energies is observed. The position of the high energy peak on the energy axis can be controlled by adjusting the low-frequency voltage pulse magnitude and duty cycle. The effects of tailoring the driving voltage waveform by adjusting these control parameters as well as its repetition rate on the plasma operation and the ion flux-energy distribution are analysed in depth. We find, e.g. that the duty cycle regime ($<40\%$ or $>60\%$) determines if the high energy ions form at the grounded or the powered electrode and that the duration of the pulse must exceed the ion energy relaxation time, on the order of 0.5 μs.

Keywords: capacitively coupled plasmas, low frequency and high voltage discharges, plasma–surface interactions, tailored voltage waveforms, plasma etching

(Some figures may appear in colour only in the online journal)

[*] Author to whom any correspondence should be addressed.

© 2022 IOP Publishing Ltd Printed in the UK

1. Introduction

Radio frequency (RF) driven capacitively coupled plasmas (CCPs) in the low pressure regime are routinely used in various surface processing technologies. Plasma-assisted chemical vapour deposition [1], plasma etching [2], doping [3], and plasma-based synthesis of nanoparticles and nanocomposite coatings [4] are just a few of the broad categories to mention, each of which finding numerous adaptations in several applications in fields like the fabrication of microelectronics, solar cells, bio-compatible and wear resistant surfaces [5–8]. Common to all of these applications is that the key parameters, determining the quality of the process, including the composition, quantity (flux) and energy distribution of reactive particles interacting with the surface of interest. In the case of charged plasma particles (electrons and ions), the time evolution of the RF sheath adjacent to the surface determines the energy distribution, while inelastic collisions (mainly electron impact ionization) are the sources, determining the density and composition, for a given buffer gas mixture. Different applications require significantly different energy distribution function shapes and particle fluxes. In deposition, for instance, the ion energy must be fine-tuned to control film characteristics (hardness, elastic modulus, composition), while the ion flux (deposition rate) should be kept constant. Applications demand the separate control of these process-critical quantities [9].

In the simplest case of single frequency RF voltage excitation, typically broad bi-modal ion energy distributions form at the electrodes and there is practically no possibility to control the ion flux and mean energy independently from each other. The variation of the voltage amplitude does directly influence the RF sheath dynamics, which, on the other hand, determines both the gas phase ionization as well as the acceleration of ions towards the surfaces. An important step towards such separate control was the introduction of dual frequency excitation, e.g. by adding a 2 MHz low-frequency component to the 27 MHz high-frequency excitation [10–13]. The governing idea is that the high-frequency component is primarily responsible for the charged particle production through sheath expansion electron power absorption, accelerating the electrons into the plasma bulk, while the (often larger amplitude) low-frequency component controls the mean sheath voltage, responsible for the acceleration of the ions to the surface. It has been shown that the separate control of the mean ion energy and flux could be realized only to some limited extent in this way, not covering a wide enough range of discharge parameters relevant to many applications [14]. The shape of the ion energy distribution function at the electrodes typically cannot be controlled in such dual-frequency CCPs.

An alternative concept was developed using a number of phase locked higher harmonics of a base frequency, sometimes referred to as the 'Fourier ansatz'. In the case of 'classical' dual frequency excitation, as discussed above, the relative phase angle between the two largely different frequency components is irrelevant. In this case, however, the variation of the relative phases between the harmonic components provides additional control over the particular shape of the applied voltage waveform, realizing a variant of 'voltage waveform tailoring' (VWT). An interesting consequence of this method is the introduction of the 'electrical asymmetry effect' [15, 16] resulting in the controllable development of a significant DC self-bias voltage even in the case of geometrically symmetric systems, as it has been shown in a series of numerical studies [17–25]. In principle, by applying a high enough number of harmonics, any arbitrary shape of the voltage waveform can be achieved, although technical limitations (frequency bandwidth, impedance matching, etc) do restrict the feasible harmonic number [26–28]. The benefits of this method have been demonstrated in sputtering experiments [29], electropositive [30] and electronegative plasmas [31], as well as for silicon thin film deposition experiments [32–34]. In case of high base frequencies, e.g. 13.56 MHz, the control of the ion flux-energy distribution function (IFEDF) at the electrode is mediated through the adjustment of the DC self-bias, since the ions typically cannot react to the instantaneous sheath electric field. Thus, only integral properties of the IFEDF can be controlled, i.e. the mean ion energy and flux. However, for a variety of applications, e.g. selectivity control in plasma etching, the shape of the IFEDF must be controlled [35–37]. Ideally, IFEDFs with narrow peaks at controllable energies are generated to activate etching of a distinct material, but not of other materials. Oftentimes, such activation energies are only about 10 eV apart. This is particularly relevant for atomic layer etching (ALE), where only the activated top layer of a wafer is supposed to be etched with high selectivity against the non-activated layer underneath.

To allow controlling the IFEDF shape, the use of non-sinusoidal low-frequency tailored voltage waveforms introduces additional degrees of freedom. Based on simulations and in remote plasma sources, such voltage waveforms were used for RF substrate biasing and were demonstrated to enhance selectivity in etching [35] and to be beneficial for doping [36]. Such remote plasma sources can be inductively coupled or helicon sources. Experiments performed in such a remote plasma source with arbitrary substrate biasing confirmed that the IFEDF can be controlled in this way [37–40]. In this case the separate control of the ion flux and IFEDF shape can be largely improved.

In this work, we pursue a combined approach, where a single high-frequency component (HF in the 10 MHz range) is complemented by a low repetition rate (LF in the 100 kHz range) tailored square-shaped voltage waveform applied to the same electrode in a purely capacitively generated plasma without remote source. As many plasma process applications are performed in such pure CCPs, such studies are important. Fundamentally, the obtained results are expected to be markedly different from those obtained in remote plasma sources, since the discharge is generated by the capacitively applied driving voltage waveform rather than a remote source, e.g. an inductively coupled or a helicon source, that results in different electron power absorption mechanisms compared to CCPs. One of the great advantages of this approach is the fact that existing commercial CCP reactors can simply be upgraded to VWT by modifying the external power supply and without changing the reactor itself. Adding a remote plasma source is typically

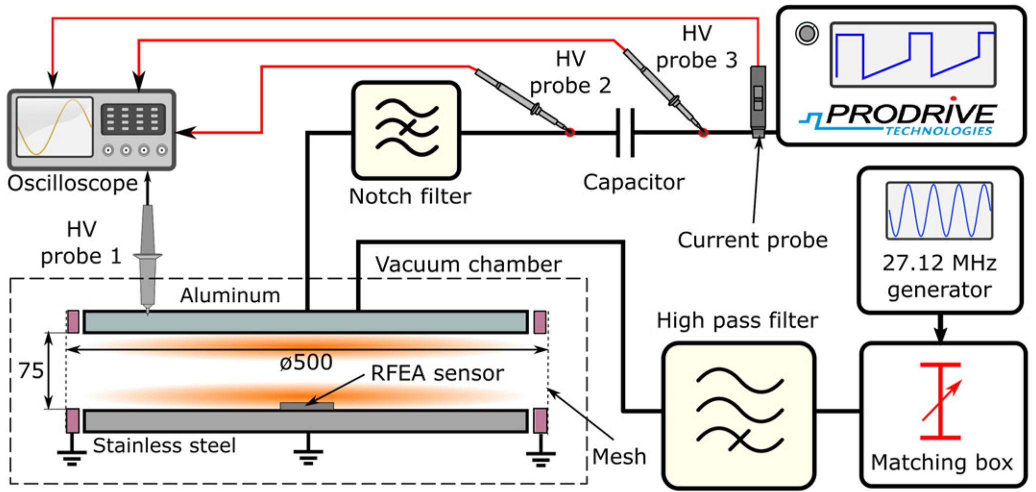

Figure 1. Schematics of the experimental setup.

not an option, since this would require a major re-design of the entire plasma source and process. In contrast to pulsed RF biasing, recently used in etching applications [41], in our case the high frequency component is permanently active, the low-frequency waveform is added to it. This should result in higher particle fluxes to the wafer and higher process rates as compared to those accessible in pulsed plasmas. Conceptually, the high-frequency component is responsible for the sustainment of the RF discharge, while the low-frequency waveform can be tuned to optimize the sheath dynamics in order to control the ion energy distribution function shape. Numerical simulations related to plasma etching and based on high voltage discharges, predicted strong benefits of this method on both the IFEDF optimization and the possibility of electron acceleration for surface charge neutralization inside a high aspect ratio etch features [42].

In this study, we present both numerical and experimental results on the DC self-bias voltage and the energy distribution of Ar^+ ions impacting the electrodes in low pressure ($p = 1$ Pa) argon CCPs in a plane-parallel electrode configuration, driven by tailored voltage waveforms composed of a single high-frequency ($f_{HF} = 27.12$ MHz) component and various pulsed low-frequency square-shaped signals with $f_{LF} = 100$ kHz repetition rate. Particle-in-cell with Monte Carlo collision treatment (PIC/MCC) simulations with both one-dimensional (1D) and cylindrical two-dimensional (2D) spatial symmetries are performed in order to complement the experiments and to provide deeper insight into the operation characteristics of the gas discharge. Starting from a base case, the effects of the variation of the LF pulse voltage amplitude, its repetition rate, and the LF duty cycle are discussed.

2. Experiments

A schematic view of the experimental set-up is depicted in figure 1. The plasma is generated inside a vacuum chamber between two plane parallel electrodes with a diameter of 490 mm. The distance between the electrodes is fixed to $L =$ 7.5 cm. To confine the active plasma volume, the electrodes are surrounded by a conductive mesh. The mesh and the bottom electrode are grounded and made of stainless steel. The upper electrode is powered and made of aluminium. The cuboid-like vacuum chamber ($L \times W \times H = 800 \times 800 \times 600$ mm^3) is pumped down to $\approx 10^{-5}$ Pa before the experiments by two turbomolecular pumps connected to a roots pump through a rotary pump. During the experiment, the pressure inside the chamber is monitored by an MKS capacitance manometer (6274BX01). In this work, the experiments are performed in high-purity (99.999%) argon gas. The gas flow and pressure are set to 40 sccm and 1 Pa, respectively. More detailed information about the vacuum and gas handling systems can be found elsewhere [29, 43, 44]. The upper electrode is powered simultaneously combining 27.12 MHz excitation frequency and pulsed low-frequency signals. The high excitation frequency is generated by a power generator (Ceasar VM2715AW, 1,5 kW) and delivered via a matching network (VarioMatch VM2715AW, 1.5 kW, Advanced Energy) and a high pass filter. The filter is custom-made (designed by Aurion) and used to protect the HF electronics components from parasitic coupling with the low-frequency signal. In the present experiment, the power of the HF generator was fixed at 60 W. The LF signal is generated by a custom-tailored waveform generator designed and produced by Prodrive Technologies. The signal is then applied via a blocking capacitor and custom-made notch filter (Prodrive Technologies) to the powered electrode. The RF notch filter is used to block 27.12 MHz and protect the LF electronics. The total applied voltage signal at the powered electrode is measured by a high voltage (HV) probe (Tektronix P6015A with a bandwidth of 75 MHz) marked as 'HV probe 1' in figure 1. The HV probe is calibrated via a procedure described by Ries *et al* [29]. The calibration is needed to obtain a correct voltage signal at the electrode surface. To monitor the voltage waveforms before the notch filter and produced directly by the LF power generator two identical high voltage probes 'HV probe 2' and 'HV probe 3' (PMK PHVS 662-L-RO) are used, respectively. In this way the efficiency of the notch filter and the performance of the Prodrive power supply are monitored during the experiments.

The LF pulse generator creates voltage waveforms (monitored by HV probe 3) with a non-zero time average. This DC offset drops across the blocking capacitor, so that the LF voltage waveform applied to the electrode, $\Phi_{\rm LF}(t)$, does not include any DC offset. The low frequency driving voltage waveform used as input for the simulations is the waveform measured by HV probe 3 with the DC component subtracted. A current probe (Tektronix TCP0030A, 120 MHz) is applied to record the current consumed by the system. The probes are connected to a digital oscilloscope (Tektronix DPO4104). The data from the oscilloscope is then recorded by a LabVIEW software. To obtain ion flux-energy distributions, a retarding field energy analyzer (RFEA) is placed at the middle of the grounded electrode. The RFEA sensor together with a holder (Impedans Ltd Semion™ single sensor) has a diameter of 70 mm and 5 mm thickness. The energy resolution of the measured data is around 1 eV, while the long time reproducibility was found to be within ± 3 eV. The operation principle of the sensor and the data evaluation procedure can be found elsewhere [45, 46]. It is to note that the connection between the RFEA signal and the ion flux-energy distribution is generally not trivial. Neglecting secondary effects inside the detector, like the secondary electron emission (SEE) induced by the impacting ions, metastable atoms, and resonant UV photons from the discharge the RFEA signal relates to the surface-normal component of the ion velocity distribution function, or in short the flux-velocity distribution, represented on the energy scale. However, in the case of a collisionless sheath, where the particles predominantly impact perpendicularly onto the electrode surface, we can assume that their total kinetic energy is carried by their surface-normal motion. In this case the flux-energy and flux-velocity distributions are equivalent and the RFEA measurements properly represent the IFEDF. A detailed analysis of the RFEA signal interpretation and calibration procedures can be found elsewhere [47, 68].

3. PIC/MCC simulations

The main simulation tool of this study is our PIC/MCC code. The popularity of the PIC method in the field of gas discharge physics started to increase rapidly after Birdsall and Langdon [48, 49] adopted the original concept [50] to electrically charged particle systems by incorporating a Monte-Carlo type collision (MCC) treatment of the interactions between charged particles and the thermal background gas into the simulation scheme. The resulting 'PIC/MCC' approach has become the most widespread method for numerical kinetic studies of CCPs over the past decades [51–58]. Recent improvements in computing capabilities, e.g. those provided by general purpose graphic processing units (GPUs), led to a drastic shortening of simulation times and made time-consuming problems tractable [59–62]. All relevant details of the current version of our GPU accelerated PIC/MCC simulation for argon gas are described in [63].

We define a reference 'base case' for the simulations with the following discharge parameters: argon gas at $p = 1$ Pa pressure and $T_{\rm g} = 350$ K temperature, the discharge gap is $L = 7.5$ cm, the electrode surfaces are identical and are characterized by a constant ion-induced electron emission (IIEE) yield $\gamma = 0.1$ and an elastic electron reflection probability $\eta_{\rm ela} = 0.5$. Numerical parameters include the number of grid points $N = 512$, the time step $\Delta t = 9.3$ ps, and a super-particle weight factor of $w = 100\,000$ per cm^2 of nominal electrode area, resulting in approx. 200 super-particles per species per cell of the numerical grid. The voltage applied to the powered electrode (at $x = 0$ coordinate) is composed of the following terms:

$$\Phi(t) = \Phi_{\rm LF}(t) + V_{\rm HF}\cos(2\pi f_{\rm HF} t) + V_{\rm DC}, \qquad (1)$$

where $V_{\rm HF} = 92$ V is the amplitude of the $f_{\rm HF} = 27.1$ MHz high-frequency component, equivalent to the $P_{\rm RF} = 60$ W RF power case in the experiments, and $V_{\rm DC}$ is the self-consistently determined DC self-bias voltage, iteratively adjusted after every $f_{\rm LF} = 100$ kHz low-frequency period ensuring the time averaged balance of charged particle currents at the electrodes. For both the LF and HF voltage waveform zero DC levels are assumed. Therefore, $V_{\rm DC}$ represents the long time average of the electrode potential. Compared to the experiments, a slightly lower HF is used, i.e. 27.1 MHz instead of 27.12 MHz, to ensure that the HF is an integer multiple of the LF in the simulation. This is done to ensure that consecutive LF periods are identical so that, based on averaging over many LF periods, meaningful HF spatio-temporally resolved data for various plasma parameters can be extracted from the simulation. The excellent agreement between computational and experimental results justifies the applicability of this approach retrospectively. For the shape of $\Phi_{\rm LF}(t)$, the low-frequency waveform, we apply two different approaches: (i) using the experimentally recorded driving voltage waveform (according to the procedure outlined in section 2), if experiments were performed under the respective discharge conditions, or (ii) generating synthetic pulses resembling potential experimental waveforms, if no experiments were performed for such waveforms, by setting both the rising-, and falling edge transition times to $t_{\rm rise} = 200$ ns. For the base case, the measured waveform with $V_{\rm LF} = 100$ V peak-to-peak voltage and $D_{\rm n} = 20\%$ duty cycle is chosen, as shown below in figure 2(a). It is to note that in the case of experimentally recorded voltage waveforms the indicated nominal value of the duty cycle corresponds to the value set at the power supply, indicated in the following by $D_{\rm n}$, while the real D value is determined by measuring the full width at half maximum of the actual LF voltage waveform. We observe a constant shift in the form of $D = D_{\rm n} + 1.8\%$ in the relation of these two definitions.

The potential uncertainties of the simulation results originate from multiple sources, such as the validity of the underlying theoretical discharge model, the accuracy of the collision cross section data used, the accuracy of the numerical solution techniques, and the statistical noise introduced by the limited number of simulation particles. A rigorous investigation involving all aspects can not be provided here, we are limited to considering only the statistical component. Based on the fluctuation of the particle number around the stationary values in the converged phase, the stochastic uncertainty

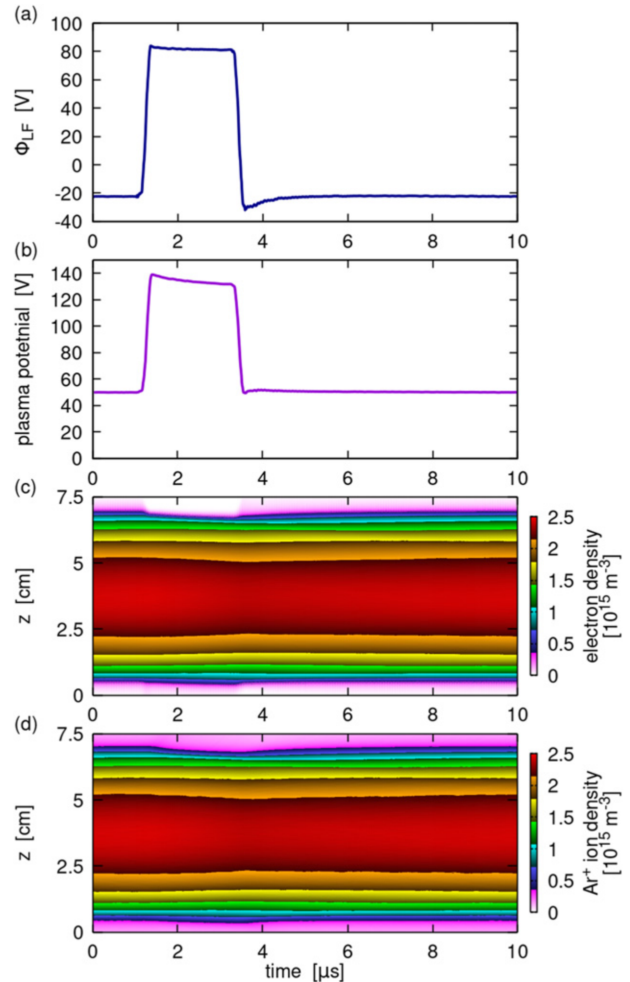

Figure 2. Time dependence of the low-frequency driving voltage waveform, $\Phi_{LF}(t)$, as recorded experimentally and used as input for the simulation (a) and the computed low-pass filtered plasma potential (b), and the electron (c) and Ar^+ ion (d) density distributions. Discharge parameters of the base case include: argon gas at $p = 1$ Pa, $L = 7.5$ cm, $V_{HF} = 92$ V, $f_{HF} = 27.1$ MHz, $V_{LF} = 100$ V, $f_{LF} = 100$ kHz, $D_n = 20\%$.

can be estimated to be around 1%. The simulation is converged, when the superparticle number is stabilized and does not change anymore apart from statistical fluctuations. Typically, 100–200 LF periods are required to reach this state. Argon metastables are neglected in our simulation. This is justified at low pressure, since the metastable density is low [69]. Even if there was a significant metastable component, due to its diffusion-limited (slow) time evolution, at the timescale of the LF excitation it would provide an excess background plasma density [70] that would not alter the conclusions of the present study.

Most of the simulation data presented throughout this work are obtained by the above-referred 1D3V (one dimensional in space and three dimensional in velocity space) simulation code, as it can capture most of the relevant physical phenomena while demanding acceptable simulation runtimes. However, the geometrical asymmetry between the grounded and powered electrodes of the experimental setup is not included in this model. The smaller powered electrode area is expected to introduce a negative offset of the DC self-bias voltages even in the case of symmetric input voltage waveforms characterized by a time average of zero. To estimate the effect of the geometrical asymmetry we have added axisymmetric 2D3V simulations with equivalent physical and numerical parameters adopting the geometry of the experiment. Technical details of our 2D3V simulation model can be found in our earlier works [64, 65]. In the present adaptation the geometry closely follows the experimental system, the powered and grounded electrodes, having diameters of $d = 492$ mm, the 1 mm gaps between the electrodes and the outer grounded holder rings, as well as the vertical grounded mesh (modelled as a solid wall) are included in the model with Dirichlet boundary conditions for the electrostatic potential calculation. The applied numerical grid has a resolution of 1024×1024 points, and the super-particle weights are set to result in approx. 40 000 000 simulation particles for each charged species.

4. Results and discussion

In this section, we first provide some insights into the operation mechanism of the discharge at the reference 'base case' conditions based on 1D PIC/MCC simulations. This is followed by the comparison of numerically and experimentally obtained IFEDFs. We discuss similarities and differences between the experimental and computational results, perform variations of the low-frequency voltage, the repetition rate, and the duty cycle. The role of the DC self-bias voltage is discussed, and finally the importance of the geometrical asymmetry of the experiment is demonstrated by adding 2D3V simulation results.

4.1. Operation principles

Being operated at low pressure, which is necessary to form a collisionless electrode sheath for the Ar^+ ions to reach high impact energies, the dominant electron power absorption mechanism is expected to be the 'sheath expansion heating', also referred to as 'α-mode operation' [66]. In this case, from the perspective of electron dynamics, and ultimately the ionization dynamics, being of paramount importance for sustaining the discharge, the motion (expansion and collapse) of the high frequency sheath plays a governing role. On the other hand, from the perspective of the ion dynamics, which is the primary focus of this work, the HF component is too fast to directly influence the ion motion. Therefore, it remains the low frequency voltage component together with the DC self-bias voltage to determine the IFEDF at the electrodes.

Figures 2(a) and (b) show the time dependence of the applied LF voltage components, $\Phi_{LF}(t)$, as recorded experimentally and used as input to the simulation, as well as the low-pass filtered plasma potential (the potential in the centre of the plasma bulk). The ions, which are leaving the bulk region, are accelerated by the sheath electric field towards the surface, and in the case of the grounded electrode, with a fixed electric potential of $\Phi(x = L) = 0$ V, the sheath potential is equal to the plasma potential.

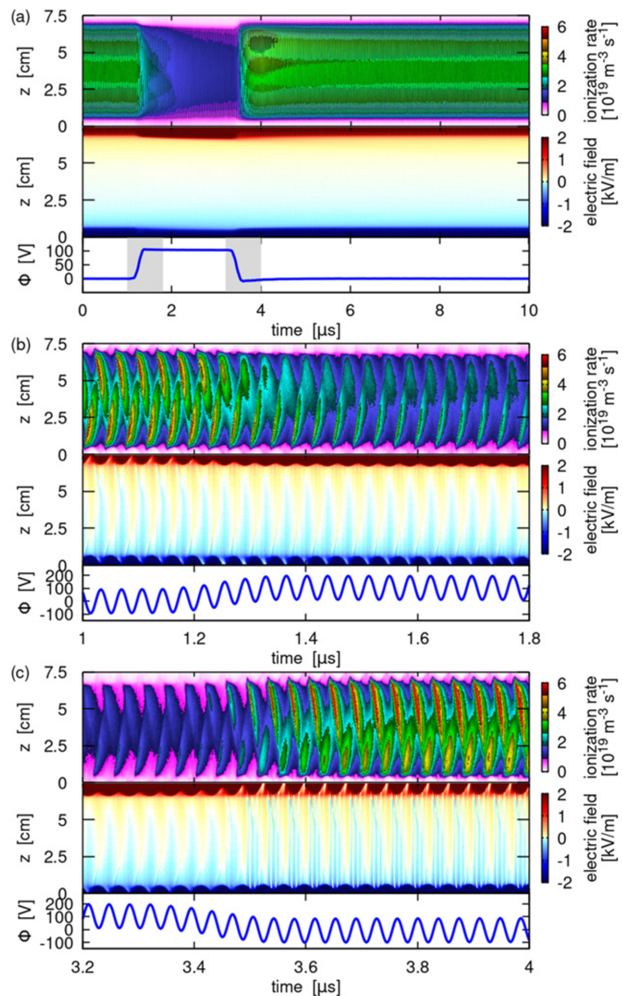

Figure 3. Spatio-temporal evolution of the ionization rate and electric field distributions as well as the time evolution of the electrode voltage. (a) Full LF period with low-pass filtered voltage, (b) and (c) high resolution zooms into the rising-, and falling edge regions. Discharge parameters as in figure 2.

Figures 2(c) and (d) show the spatio-temporal distributions of the electron and Ar^+ ion densities, respectively. Focussing on the boundary regions it is visible that electrons do react to the HF sheath motion, and, during the majority of the time, have a chance to reach the surfaces during phases of HF sheath collapse and are pushed towards the bulk during HF sheath expansion. In contrast, the ions, due to their high inertia, are unable to respond at the HF timescale. However, some interesting details can be observed here, which are not common to high frequency (>10 MHz) harmonic voltage driven discharges. During the period of positive LF pulse the sheath remains fully expanded at the grounded side, the HF oscillation can not compensate for the high LF voltage, and therefore, even during the HF sheath collapse phase, the electrons are strongly repelled from and the ions are accelerated to the surface. This introduces an imbalance, as on the opposing powered side, the sheath becomes narrower and electrons are efficiently drained towards the powered electrode. The increased loss of ions at the grounded and the efficient escape of electrons on the powered side result in a decrease of the plasma density on the order

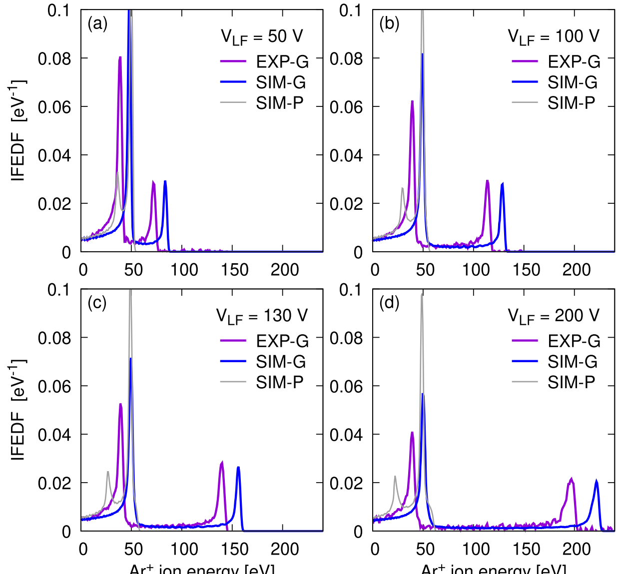

Figure 4. Experimental (EXP) and computed (SIM) IFEDFs at four different low-frequency voltage magnitudes normalized so that $\int \mathrm{IFEDF}(\varepsilon)\mathrm{d}\varepsilon = 1$. Numerical results include both the grounded (G) and powered (P) electrodes. Common discharge parameters are: argon gas at $p = 1$ Pa, $L = 7.5$ cm, $V_{\mathrm{HF}} = 92$ V, $f_{\mathrm{HF}} = 27.1/27.12$ MHz (SIM/EXP), $f_{\mathrm{LF}} = 100$ kHz, $D_{\mathrm{n}} = 20\%$.

of 10% by the end of the positive pulse. In addition, due to the asymmetry induced by the positive pulse, the plasma density profile shifts slightly towards the powered electrode increasing the ion density near this surface. Once the sheath expands at the powered electrode, ions located in vicinity of this boundary surface are accelerated towards this electrode and, thus, the ion density adjacent to this surfaces decreases shortly after the end of the positive voltage pulse.

Figure 3 shows the time evolution of the spatial distribution of the ionization rate, the electric field, and as reference the voltage at the powered electrode. Panel (a) provides a global view covering the full LF period and showing the low-pass filtered voltage waveform for clarity, while panels (b) and (c) show high resolution results zoomed into time intervals in the close vicinity of the rising and falling edge transitions of $\Phi_{\mathrm{LF}}(t)$, respectively. Figure 3(a) clearly shows that during the positive pulse period the global ionization rate significantly drops with respect to its value before the pulse. Panel (b) in figure 3 reveals that before the positive voltage pulse the discharge operated very symmetrically, the HF voltage component oscillated around 0 V average, assisted by the development of a DC self-bias voltage of $V_{\mathrm{DC}} = 21.6$ V. In this case, both sheaths exhibit similar dynamics contributing to the electron power absorption, and consequently to the ionization in equal shares. With the appearance of the positive voltage pulse this symmetry breaks, the dynamics of the permanently expanded sheath at the grounded electrode is largely reduced, since the HF sheath oscillation is pushed away from the electrode into a region of higher ion density. For a given HF voltage, this effect—known as frequency coupling [14]—leads to a reduction of the HF sheath width, sheath expansion velocity, and, thus, of the sheath expansion heating of electrons. Due

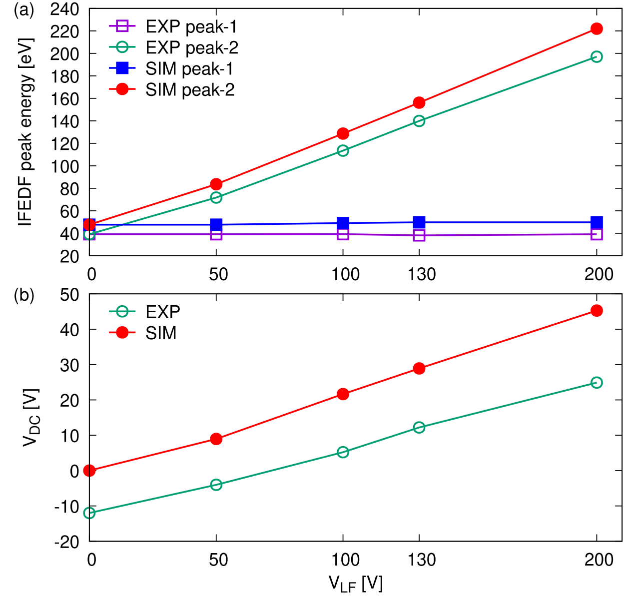

Figure 5. (a) Peak energies vs V_{LF} from experimental (EXP) and computed (SIM) IFEDFs at the grounded electrode. (b) V_{DC} (DC self-bias voltage) vs V_{LF}. Discharge parameters are the same as in figure 4.

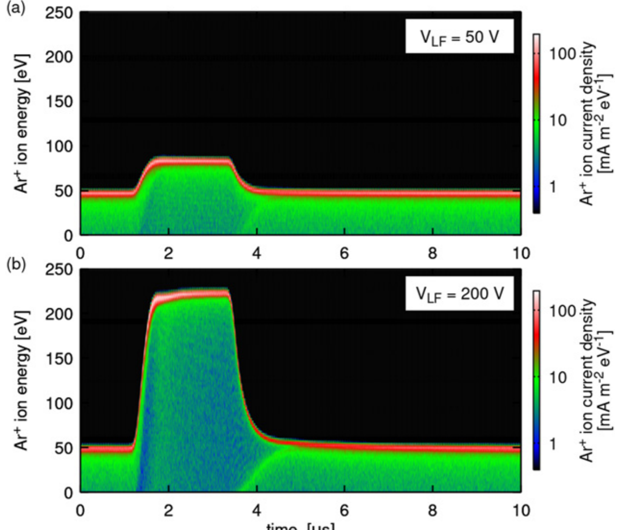

Figure 6. Computed time resolved IFEDF at the grounded electrode for $V_{LF} = 50$ V (a), and $V_{LF} = 200$ V (b). The other discharge parameters are the same as in figure 4.

to the voltage asymmetry and the shifted plasma density, the width of the powered sheath is reduced as well. As a result, the sheath expansion heating at both electrodes becomes less efficient, which further contributes to the decay of the plasma density during the pulse, as observed in figures 2(c) and (d).

Following the falling edge transition, as shown in detail in figure 3(c), a transient period, lasting a few tens of HF cycles, appears showing an enhanced magnitude and spatial asymmetry of the ionization rate distribution, together with the self-excitation of very high frequency plasma series resonance (PSR) oscillations. Although after the pulse the voltage waveform returns to a symmetric HF oscillation, the asymmetry of the plasma density can not relax as quickly due to the high ion inertia. The wide, ion-poor sheath at the grounded side experiences longer displacements during HF expansion-collapse periods, while the edge of the shorter, ion-rich sheath at the powered electrode moves only shorter distances. This transient asymmetry of the sheath, and with this the sheath capacitance, favours the excitation of the PSR with decreasing intensity as the symmetry is restored over time [67].

The above described details are somewhat modified if the geometrical asymmetry is taken into account, as it is the case in our 2D3V simulations. Here, during the off-pulse period the discharge operation is not symmetric, and PSR oscillations are more easily excited by both the rising and falling edge transitions.

4.2. Ion flux-energy distribution functions

The primary focus of the present work is on the formation and optimization of the IFEDFs, being a crucial parameter in numerous surface treatment applications. Its precise control enables cutting-edge applications like selective ALE [37]. In many cases, the optimizations aim at the formation of narrow, monoenergetic peaks in the IFEDF with full control over the position (energy) and the magnitude (flux).

In this section, we compare our experimental and computational IFEDF data, analyse the results, show the effect of the variation of the tailored voltage waveform, and discuss the importance of the DC self-bias voltage.

4.2.1. Voltage pulse magnitude variation. Figure 4 shows experimental and computed IFEDFs for four selected cases. The data in panel (b) correspond to the base case introduced above, while panels (a), (c), and (d) differ only in the values of V_{LF}, covering the range between $V_{LF}^{(a)} = 50$ V and $V_{LF}^{(d)} = 200$ V. In the experiments the RFEA measurements were restricted to the grounded electrode (G), correspondingly the numerical results focus on that side as well. The computed IFEDFs at the powered side (P) are shown for completeness without in-depth analysis.

Both the experimental and computed IFEDFs show equivalently a bimodal distribution, with a distinct low energy peak (referred to as 'peak-1') and a high energy companion (referred to as 'peak-2') at the grounded electrode. Peak-1 shows no sensitivity on V_{LF} at all, while the position of peak-2 scales linearly with V_{LF}, as visible also in figure 4(a). Despite the perfect qualitative agreement between the experimental and numerical distributions, a systematic shift on the order of 10–20 eV is present in the numeric data towards higher energies. Further, at the powered electrode side, the formation of two peaks is observed, however in this case the peak at higher energy is equivalent to peak-1, while the other peak forms at lower energies with increasing V_{LF}.

Figure 5(a) shows a comparison of the energies of the peaks in the IFEDFs vs V_{LF}, confirming the above described observations at the grounded electrode. To shed light on the observed energy shift between the measured and computed peak energies, figure 5(b) depicts the experimental and numerical V_{DC} DC self-bias voltages. As expected, at $V_{LF} = 0$ V, when the

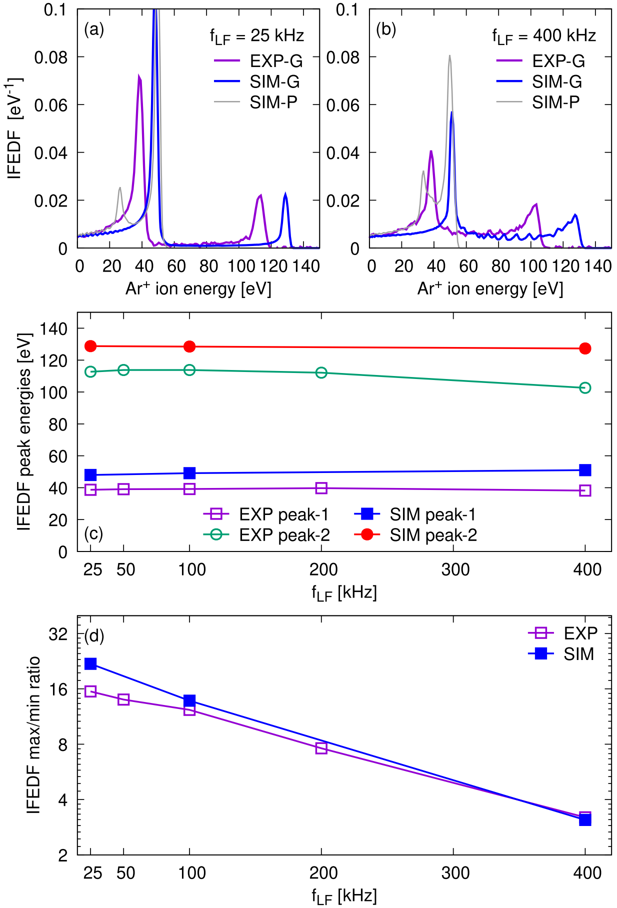

Figure 7. Experimental (EXP) and computed (SIM) IFEDFs for $f_{LF} = 25$ kHz (a) and $f_{LF} = 400$ kHz (b). (c) Peak energies vs f_{LF} from experimental (EXP) and computed (SIM) IFEDFs at the grounded electrode. (d) Intensity ratio of the peak-2 amplitude and the minimum intensity measured halfway between peak-1 and peak-2. Other discharge parameters are the same as in figure 2.

applied voltage waveform contains only a single HF harmonic component, the 1D3V PIC/MCC simulation predicts $V_{DC} = 0$ V, as the model does not contain any explicit asymmetries. In contrast to the simulations, the experiment shows a negative self-bias, which is expected in the case of the geometrical asymmetry present in the system (different effective grounded and powered electrode areas) even in the case of a harmonic driving voltage. In addition to the geometrical asymmetry, in the experiment, the powered electrode is made of aluminium, while the grounded electrode is stainless steel. Earlier studies have shown that such material asymmetry, especially at high voltage conditions, can induce significant DC self-bias formation [63]. Depending on the effective IIEE, as well as the electron impact SEE yields of the opposing surfaces the contribution to V_{DC} can be positive or negative. For the present configuration, we expect a small positive effect of the material asymmetry on the DC self-bias voltage. Although our PIC/MCC simulation contains a simple model for both IIEE and SEE, as introduced in section 3, the same coefficients are used for both electrodes.

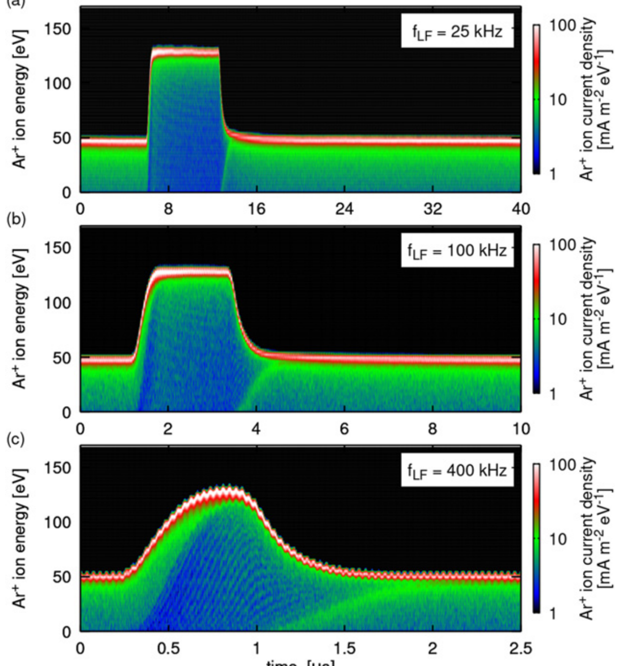

Figure 8. Computed time resolved IFEDF at the grounded electrode for the $f_{LF} = 25$ kHz (a), $f_{LF} = 100$ kHz (b), and $f_{LF} = 400$ kHz (c). Other discharge parameters are the same as in figure 2.

Figure 5 shows that the difference in V_{DC} between the experiments and the simulations shows only a slight dependence on V_{LF} and apparently directly corresponds to the observed energy differences of the IFEDFs peaks. We recall that the ions are accelerated towards the electrodes by the sheath voltage, which is the difference between the plasma potential and the surface potential (which is zero at the grounded side). Although the formation of the plasma potential is a complex phenomenon, at the timescale of the ion dynamics, and as long as $|V_{DC}| \ll V_{HF}$ or $|V_{DC}| \ll V_{LF}$ a linear connection (with offset) between V_{DC} and the plasma potential can be assumed. In this case, a direct connection between the DC self-bias voltage and the energy shift in the IFEDFs can be drawn, predicting the primary reason for the observed energy difference between experiment and simulations to be the missing asymmetries in the simulations.

Further, it is interesting to note that the computed DC self-bias voltages, as shown in figure 5(b), have in common that the actual values effectively compensate the contribution of the positive voltage pulse with respect to the time average of Φ_{LF}. As a result, a baseline voltage of $\approx$0 V develops, as appears in figure 3, providing symmetric discharge operation outside the positive pulse. This behaviour is observed in the case of $D \leqslant 30\%$, and will be discussed in more detail below together with the effect of duty-cycle variation.

Figure 6 shows the time resolved IFEDF at the grounded electrode for the $V_{LF} = 50$ V and 200 V cases, the corresponding data for the original base case ($V_{LF} = 100$ V) appears below in figure 8(b). We observe that two distinct time

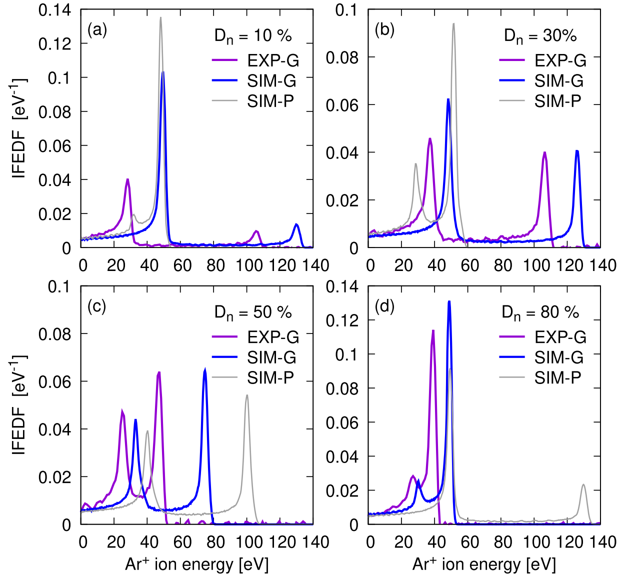

Figure 9. Experimental (EXP) and computed (SIM) IFEDFs at four different duty cycles normalized so that $\int$ IFEDF(ε)d$\varepsilon = 1$. Numerical results include both the grounded (G) and powered (P) electrodes. Common discharge parameters are: argon gas at $p = 1$ Pa, $L = 7.5$ cm, $V_{\mathrm{HF}} = 92$ V, $f_{\mathrm{HF}} = 27.1/27.12$ MHz (SIM/EXP), $V_{\mathrm{LF}} = 100$ V, $f_{\mathrm{LF}} = 100$ kHz.

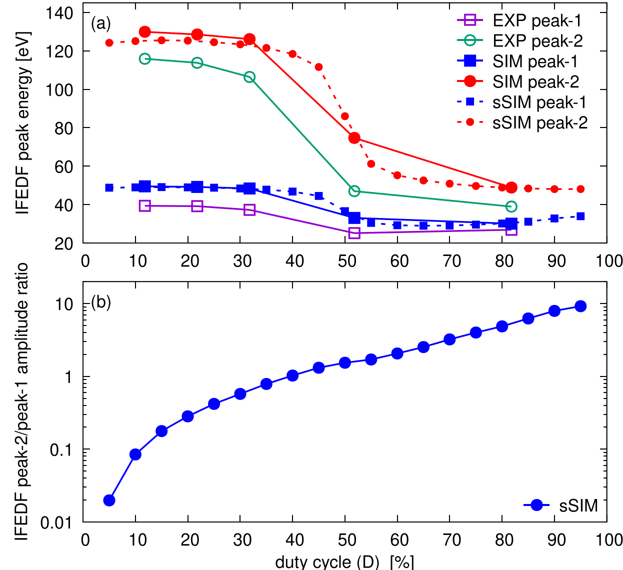

Figure 10. IFEDF peak positions (a), and peak-2/peak-1 magnitude ratios (b) vs duty cycle D. Plotted are experimental results (EXP), 1D3V PIC/MCC simulations using LF voltage waveforms recorded from the corresponding experiments (SIM), as well as using synthetic LF pulses (sSIM). Discharge parameters are the same as in figure 9.

intervals, corresponding to the base and the positive pulse LF voltage periods, form and show stationary character (energy plateaus) with peaking current intensities at the high sides of the instant distributions. The duration of the transient period between the two plateau regions is on the order of $\approx$0.5 μs on the rising-edge side and slightly longer at the falling-edge side, limited by the ion response time. The stability of the peak energy values results in the observed sharpness of the peaks in the IFEDFs, as shown in figure 4. The position (on the energy scale) of the peaks is directly related to the plateau values of the plasma potential, as shown in figure 2(b).

4.2.2. Repetition rate variation. A valid question at this point of the analysis could be related to the choice of the low-frequency repetition rate. $f_{\mathrm{LF}} = 100$ kHz was picked for the base case, and both experiments and simulations were performed to justify this choice. Figures 7(a) and (b) compare IFEDF data for $f_{\mathrm{LF}} = 25$ kHz and 400 kHz, respectively, at otherwise base case identical discharge conditions. Besides the already discussed energy shift between the experimental and 1D3V simulation results, and the slightly sharper peak-1 due to the higher energy resolution of the simulations, the governing features are very well captured by the computations. We observe that the IFEDFs up to the first peak, including the width of peak-1, are largely insensitive to the LF repetition rate. However, the base intensity between the low-, and high energy peaks, as well as the shape and amplitude of peak-2 show pronounced variations with f_{LF}. From figure 7(c) we can conclude that the positions of the spectral peaks in the IFEFDs show only small sensitivity, reducing the energy only at the highest LF repetition rate of $f_{\mathrm{LF}} = 400$ kHz and only for peak-2. On the other hand, as depicted in figure 7(d), the magnitude ratio of the high-energy peak to the mean value, measured halfway between peak-1 and peak-2, clearly shows the increasing population of intermediate energy ions that continuously fill up the spectral range between the peaks at the expense of the high-energy peak.

To aid the understanding of the observed f_{LF} dependence, figure 8 shows the time evolution of the IFEDF at the grounded electrode for different LF repetition rates. As discussed above, for the formation of sharp, large amplitude peaks in the IFEDF, long and stationary plateau regions are necessary. Apparently, with increasing the repetition rate, at fixed duty cycles, the duration of the positive voltage pulse becomes too short for the ions to reach a stationary transport state and no extended plateau can form. As a result, ions with all possible energies between the base and the peak values arrive at the electrode in high quantities. This phenomenon, originating from the high ion inertia, places an upper limit to the LF repetition rate to provide the desired IFEDF shape. There is, on the other hand, a practical lower limit for f_{LF} originating from the external electrical circuit properties. RF CCPs are generally powered through an impedance matching network, which contains a blocking capacitor preventing DC currents to flow. In the present simulations, this blocking capacitor is assumed to be large enough that during a single LF period, regardless of the magnitude of the instant discharge current, its voltage, and with this, the DC self-bias voltage, remains unchanged. Adjustment steps of the DC self-bias voltage are performed only after each LF period, ensuring zero DC current on the long time average. In the experiments, the voltage drop on the blocking capacitor can change, especially if the

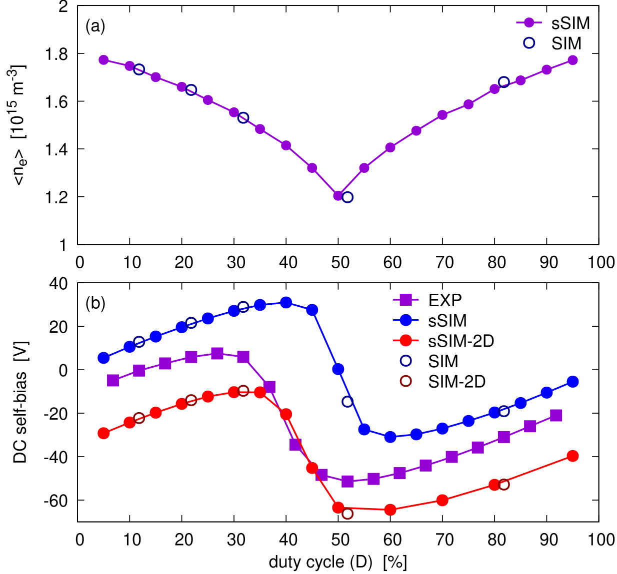

Figure 11. Computed mean electron density (a) and DC self bias voltage (b) from the experiment (EXP), 1D3V PIC/MCC simulations (SIM and sSIM), and 2D3V PIC/MCC simulations (SIM-2D and sSIM-2D) as functions of the duty cycle. Discharge parameters are the same as in figure 9.

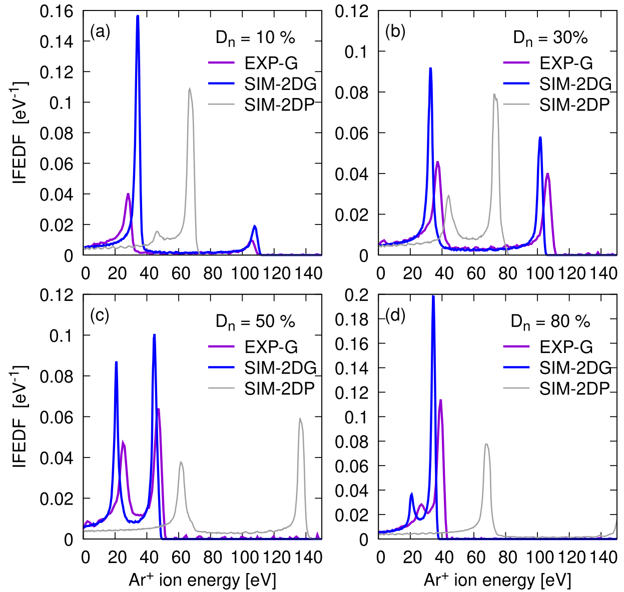

Figure 12. Experimentally (EXP) and computationally (2D3V PIC/MCC, SIM-2D) obtained IFEDFs at four different duty cycles normalized so that $\int$ IFEDF(ε)dε = 1. Numerical results include both the grounded (G) and powered (P) electrodes. Discharge parameters are the same as in figure 9.

unidirectional currents, e.g. during the positive voltage pulse, persist for extended times, resulting in distortions of the IFEDFs. Overall, these results show the LF repetition rate should be selected from a distinct interval to ensure the presence of a sharp high energy IFEDF peak and a strongly reduced ion current at intermediate energies. This is important for various applications such as selective etching and typically cannot be realized by classical sinusoidal driving voltage waveforms. For most discharge conditions the ideal LF repetition rate is expected to be about 100 kHz.

4.2.3. Duty cycle variation. Besides the magnitude V_{LF} and the repetition rate f_{LF}, the third trivial tuning parameter is the duty cycle D of the LF voltage pulse. Based on the insights so far one would expect that by varying the length of the positive voltage pulse within the LF cycle the ratio of the high-, and low energy peak magnitudes can be tuned. Of course, it would be naive to expect that with the variation of the duty cycle the position of the IFEDF peaks remains unaffected. Therefore, in the remaining part of this study we focus on the complex consequences of a duty cycle variation.

Figure 9 collects the experimentally available IFEDFs for the cases derived from the original base case by varying only the duty cycle of the low-frequency pulsed voltage waveform. Comparing the low duty cycle cases $D_{\mathrm{n}} = 10\%$ (panel (a)), $D_{\mathrm{n}} = 20\%$ (figure 4(b)), and $D_{\mathrm{n}} = 30\%$ (panel (b)) the above formulated expectations, regarding the variation of the peak magnitudes and the stability of the peak positions seem to be justified. At larger duty cycles, however, the onset of a significant transformation can be observed. It is to note here, that due to the perfect symmetry of the 1D3V PIC/MCC simulations, the high-, and low duty cycle cases operate as inverses of each other, in the way that e.g. the $D = 20\%$ case is equivalent to the $D = 80\%$ case, just with reversed electrode assignments. This can be seen comparing the IFEDF at the powered electrode in figure 9(d) with the base case data shown in figure 4(b) at the grounded side.

Figure 10 shows an analysis of the IFEDF peak positions and the magnitude ratios of the high-, and low-energy peaks in panels (a) and (b), respectively. The plots show data derived from RFEA measurements and 1D3V PIC/MCC simulations using LF voltage waveforms recorded from the corresponding experiments. To improve the resolution along the duty cycle axis, 1D3V PIC/MCC computations using synthetically generated (simple symmetric square pulses with 200 ns rise and fall times) LF waveforms are added to the results. There is only a negligible difference between the results obtained with the two numerical approaches, therefore no distinction will be made during the following discussion. Both the experimental and numerical results verify the stability of the peak energies up to $D \leqslant 30\%$ for the experiment and $D \leqslant 40\%$ in the case of the simulations. At the large duty cycle side, above $D \geqslant 60\%$ we find that peak-2 settles at the position of the former peak-1 feature, which, on the other hand, shifts towards even lower energies. Regarding the evolution of the relative peak magnitudes, panel (b) confirms that by adjusting the duty cycle the ratio of the low-, and high-energy ion populations can be sensitively tuned.

Ideally, one aims at the complete decoupling of the plasma generation from the IFEDF control. As a function of the duty cycle the plasma density, as shown in figure 11(a) for the mean electron density, does vary about $\pm 20\%$ around the middle value, however, as discussed above, in the practically useful range $10\% < D < 40\%$ the variation is reduced to only $\pm 10\%$, which might be small enough for practical purposes.

As already introduced earlier, the DC self-bias voltage is a discharge parameter that (1) is very easy to measure, (2) is very sensitive to any kind of (geometrical-, electrical-, or material-) asymmetries, and (3) has a very direct influence on the impact energy of the charged particles reaching the electrodes, especially the IFEDF. Figure 11(b) shows the measured and computed DC self-bias voltage as a function of the duty cycle. As the 1D3V simulations do not contain any explicit asymmetries, V_{DC} is expected to be zero at $D = 0$, 50, and 100%, and to be symmetric around $D = 50\%$, matching the results in figure 11(b). The experimental data, on the other hand, show two systematic shifts with respect to this idealized system. The vertical shift towards lower voltages has already been discussed above and is usually attributed to the geometrical asymmetry, a larger effective grounded area with respect to the powered electrode. The fact, that besides the expected vertical voltage shift, a horizontal shift of the crossing point towards lower D values appears, suggests that the interplay of the electric asymmetry of the applied voltage waveform with the other (geometrical and material) asymmetries has a complex effect on the discharge operation.

In order to clarify if the geometrical asymmetry of the experimental systems is responsible for both vertical and horizontal shifts, we have added the results of 2D3V axisymmetric PIC/MCC simulations, with parameters otherwise identical to the 1D3V simulations, to figure 11(b). The comparison confirms that both the vertical and horizontal displacement of the V_{DC} curves are consequences of the geometrical asymmetry of the experimental setup. Consequently, the IFEDFs computed with the 2D3V simulations show remarkably better agreement with the experimental data, as shown in figure 12, where the distribution of the impacting ions is collected in the central region ($r \leqslant 10$ cm) of the corresponding electrode. As already suggested by the DC self-bias voltage data in figure 11(b), the 2D3V results slightly underestimate the positions of the peaks. The computed peak-2 energy is closest to the experimental value at 50% duty cycle, where the gap to the 1D3V computation was the largest. Another consequence of the 2D geometry is the asymmetry in the relation of the powered and grounded electrodes. With respect to the 1D3V results, while the IFEDFs at the grounded electrode shifted to lower energies, the shift to higher energies at the powered electrode can be observed when comparing figures 12 and 9, all mediated by the negative shift of the DC self-bias voltage and the larger sheath potential at the powered side.

We attribute the remaining difference between the measured and computed DC self-bias voltages to the difference of surface materials of the grounded (st. steel) and the powered (aluminium) electrodes, as well as to the mesh structure of the grounded confining cylinder, which are not included accurately in the simulations, as shown in figure 1.

5. Summary

In this, combined experimental and numerical, study of capacitively coupled RF, low pressure gas discharges, we have shown that with applying tailored voltage waveforms, composed of low frequency (LF, $\sim$100 kHz) pulsed and high-frequency (HF, $>$10 MHz) components, it is possible to efficiently decouple plasma generation from the shaping of the IFEDF at the electrodes. In particular and in contrast to classical CCPs operated at sinusoidal voltage waveforms, a sharp high energy peak can be generated with very low ion flux at intermediate energies. The peak value and energy position of this peak can be controlled efficiently by tailoring the driving voltage waveform. This is expected to be highly beneficial for a variety of applications such as selective plasma etching. More detailed findings include:

- At low duty cycles ($D \leqslant 30\%$), during the off-pulse period the discharge operates similarly to a single frequency system. During the positive voltage pulse a strong sheath asymmetry develops, since the LF sheath is fully expanded at the grounded electrode and fully collapsed at the powered electrode. Consequently, the plasma potential rises significantly and the charged particles are efficiently drained towards the electrodes.
- During the positive pulse, as a consequence of the sheath asymmetry, the sheath expansion electron power absorption mechanism becomes less efficient, resulting in a transient reduction of the plasma density.
- A bi-modal structure of the IFEDF forms with peak energies corresponding to the sheath potentials during and after the LF voltage pulse.
- The variation of the LF voltage pulse magnitude couples linearly to the position of the high-energy peak, while is not affecting the low-energy peak of the IFEDF at the grounded electrode.
- The peak to background ratio (contrast) of the high-energy peak of the IFEDF at the grounded electrode depends on the LF repetition rate, placing a practical upper limit to it for generating a sharp high energy peak.
- The duty cycle of the LF voltage pulse controls the relative magnitudes of the low-, and high-energy peaks of the IFEDFs. Two regimes, characterized by $D < 40\%$ and $D > 60\%$ are separated by a transition region. Within each, low and high duty cycle regime, individually, the positions of the spectral peaks are mostly unaffected by D.
- The DC self-bias voltage has a direct influence on the peak energies in the IFEDFs. It is a parameter sensitive to any kind of asymmetries in the system. Its complex dependence on the duty cycle was used to validate different numerical approaches.

Acknowledgments

Financial support from Prodrive Technologies B.V. is gratefully acknowledged.

Data availability statement

The data that support the findings of this study are available upon reasonable request from the authors.

ORCID iDs

P Hartmann https://orcid.org/0000-0003-3572-1310
I Korolov https://orcid.org/0000-0003-2384-1243
J Schulze https://orcid.org/0000-0001-7929-5734

References

[1] Sherman A 1984 *Thin Solid Films* **113** 135–49
[2] Cardinaud C, Peignon M C and Tessier P Y 2000 *Appl. Surf. Sci.* **164** 72–83
[3] Felch S, Fang Z, Koo B W, Liebert R, Walther S and Hacker D 2002 *Surf. Coat. Technol.* **156** 229–36
[4] Choukourov A and Mangolini L 2020 *Plasma Process. Polym.* **17** 2090003
[5] Lieberman M A and Lichtenberg A J 2005 *Principles of Plasma Discharges and Materials Processing* 2nd edn (New York: Wiley)
[6] Chabert P and Braithwaite N 2011 *Physics of Radio-Frequency Plasmas* (Cambridge: Cambridge University Press)
[7] Makabe T and Petrovic Z L 2014 *Plasma Electronics: Applications in Microelectronic Device Fabrication* 2nd edn (Boca Raton, FL: CRC Press)
[8] Chabert P, Tsankov T V and Czarnetzki U 2021 *Plasma Sources Sci. Technol.* **30** 024001
[9] Economou D J 2013 *J. Vac. Sci. Technol.* A **31** 050823
[10] Lee J K, Babaeva N, Kim H C, Manuilenko O and Shon J W 2004 *IEEE Trans. Plasma Sci.* **32** 47–53
[11] Karkari S K and Ellingboe A R 2006 *Appl. Phys. Lett.* **88** 101501
[12] Booth J P, Curley G, Marić D and Chabert P 2009 *Plasma Sources Sci. Technol.* **19** 015005
[13] Bi Z, Liu Y, Jiang W, Xu X and Wang Y 2011 *Curr. Appl. Phys.* **11** S2–8
[14] Schulze J, Donkó Z, Schüngel E and Czarnetzki U 2011 *Plasma Sources Sci. Technol.* **20** 045007
[15] Heil B G, Czarnetzki U, Brinkmann R P and Mussenbrock T 2008 *J. Phys. D: Appl. Phys.* **41** 165202
[16] Schulze J, Schüngel E and Czarnetzki U 2009 *J. Phys. D: Appl. Phys.* **42** 092005
[17] Schulze J, Schüngel E, Donkó Z and Czarnetzki U 2011 *Plasma Sources Sci. Technol.* **20** 015017
[18] Schüngel E *et al* 2016 *J. Phys. D: Appl. Phys.* **49** 265203
[19] Doyle S J, Lafleur T, Gibson A R, Tian P, Kushner M J and Dedrick J 2017 *Plasma Sources Sci. Technol.* **26** 125005
[20] Krüger F, Wilczek S, Mussenbrock T and Schulze J 2019 *Plasma Sources Sci. Technol.* **28** 075017
[21] Derzsi A, Horváth B, Donkó Z and Schulze J 2020 *Plasma Sources Sci. Technol.* **29** 074001
[22] Krüger F, Lee H, Nam S K and Kushner M J 2021 *Plasma Sources Sci. Technol.* **30** 085002
[23] Masheyeva R U, Dzhumagulova K N, Myrzaly M, Schulze J and Donkó Z 2021 *AIP Adv.* **11** 075024
[24] Wang L, Hartmann P, Donkó Z, Song Y H and Schulze J 2021 *Plasma Sources Sci. Technol.* **30** 054001
[25] Lafleur T 2015 *Plasma Sources Sci. Technol.* **25** 013001
[26] Franek J, Brandt S, Berger B, Liese M, Barthel M, Schüngel E and Schulze J 2015 *Rev. Sci. Instrum.* **86** 053504
[27] Schmidt F, Schulze J, Johnson E, Booth J P, Keil D, French D M, Trieschmann J and Mussenbrock T 2018 *Plasma Sources Sci. Technol.* **27** 095012
[28] Wang J, Dine S, Booth J P and Johnson E V 2019 *J. Vac. Sci. Technol.* A **37** 021303
[29] Ries S, Banko L, Hans M, Primetzhofer D, Schneider J M, Ludwig A, Awakowicz P and Schulze J 2019 *Plasma Sources Sci. Technol.* **28** 114001
[30] Berger B, Brandt S, Franek J, Schüngel E, Koepke M, Mussenbrock T and Schulze J 2015 *J. Appl. Phys.* **118** 223302
[31] Brandt S *et al* 2016 *Plasma Sources Sci. Technol.* **25** 045015
[32] Wang J, Longeaud C, Ventosinos F, Daineka D, Yaakoubi M E and Johnson E V 2016 *Phys. Status Solidi* C **13** 735–9
[33] Wang J K and Johnson E V 2016 *Plasma Sources Sci. Technol.* **26** 01LT01
[34] Wang J, Daineka D, Elyaakoubi M and Johnson E V 2019 *Sol. Energy Mater. Sol. Cells* **190** 65–74
[35] Agarwal A and Kushner M J 2005 *J. Vac. Sci. Technol.* A **23** 1440–9
[36] Agarwal A and Kushner M 2005 *IEEE Trans. Plasma Sci.* **33** 252–3
[37] Faraz T, Verstappen Y G P, Verheijen M A, Chittock N J, Lopez J E, Heijdra E, van Gennip W J H, Kessels W M M and Mackus A J M 2020 *J. Appl. Phys.* **128** 213301
[38] Ohmori T and Makabe T 2008 *Applied Surface Sci.* **254** 3696–709
[39] Buzzi F L, Ting Y H and Wendt A E 2009 *Plasma Sources Sci. Technol.* **18** 025009
[40] Qin X V, Ting Y H and Wendt A E 2010 *Plasma Sources Sci. Technol.* **19** 065014
[41] Yoon M Y, Yeom H J, Kim J H, Chegal W, Cho Y J, Kwon D C, Jeong J R and Lee H C 2021 *Phys. Plasmas* **28** 063504
[42] Hartmann P *et al* 2021 *J. Phys. D: Appl. Phys.* **54** 255202
[43] Bienholz S, Bibinov N and Awakowicz P 2013 *J. Phys. D: Appl. Phys.* **46** 084010
[44] Bienholz S, Styrnoll T and Awakowicz P 2014 *J. Phys. D: Appl. Phys.* **47** 065201
[45] Gahan D, Dolinaj B and Hopkins M B 2008 *Rev. Sci. Instrum.* **79** 033502
[46] Gahan D, Daniels S, Hayden C, Sullivan D O and Hopkins M B 2011 *Plasma Sources Sci. Technol.* **21** 015002
[47] Ries S, Schroeder M, Woestefeld M, Corbella C, Korolov I, Awakowicz P and Schulze J 2021 *Rev. Sci. Instrum.* **92** 103503
[48] Birdsall C and Langdon A 1991 *Plasma Physics via Computer Simulation* (Boca Raton, FL: CRC Press)
[49] Birdsall C K 1991 *IEEE Trans. Plasma Sci.* **19** 65–85
[50] Evans M W and Harlow F H 1957 The particle-in-cell method for hydrodynamic calculations *Technical Report LA-2139* (Los Alamos, New Mexico: Los Alamos Scientific Laboratory) https://apps.dtic.mil/dtic/tr/fulltext/u2/a384618.pdf
[51] Hockney R and Eastwood J 1988 *Computer Simulation Using Particles* (London: Taylor and Francis)
[52] Diomede P, Capitelli M and Longo S 2005 *Plasma Sources Sci. Technol.* **14** 459–66
[53] Matyash K, Schneider R, Taccogna F, Hatayama A, Longo S, Capitelli M, Tskhakaya D and Bronold F X 2007 *Contrib. Plasma Phys.* **47** 595–634
[54] Donkó Z 2011 *Plasma Sources Sci. Technol.* **20** 024001
[55] Donkó Z, Schulze J, Czarnetzki U, Derzsi A, Hartmann P, Korolov I and Schüngel E 2012 *Plasma Phys. Control. Fusion* **54** 124003
[56] Sun A, Becker M M and Loffhagen D 2016 *Comput. Phys. Commun.* **206** 35–44

[57] Surendra M and Graves D B 1991 *IEEE Trans. Plasma Sci.* **19** 144–57
[58] Verboncoeur J P 2005 *Plasma Phys. Control. Fusion* **47** A231–60
[59] Mertmann P, Eremin D, Mussenbrock T, Brinkmann R P and Awakowicz P 2011 *Comput. Phys. Commun.* **182** 2161–7
[60] Claustre J, Chaudhury B, Fubiani G, Paulin M and Boeuf J P 2013 *IEEE Trans. Plasma Sci.* **41** 391–9
[61] Hur M Y, Kim J S, Song I C, Verboncoeur J P and Lee H J 2019 *Plasma Res. Express* **1** 015016
[62] Juhasz Z, Durian J, Derzsi A, Matejčík Š, Donkó Z and Hartmann P 2021 *Comput. Phys. Commun.* **263** 107913
[63] Hartmann P *et al* 2020 *Plasma Sources Sci. Technol.* **29** 075014
[64] Hartmann P, Rosenberg M, Juhasz Z, Matthews L S, Sanford D L, Vermillion K, Carmona-Reyes J and Hyde T W 2020 *Plasma Sources Sci. Technol.* **29** 115014
[65] Wang L, Hartmann P, Donkó Z, Song Y H and Schulze J 2021 *Plasma Sources Sci. Technol.* **30** 085011
[66] Belenguer P and Boeuf J P 1990 *Phys. Rev.* A **41** 4447–59
[67] Mussenbrock T, Brinkmann R P, Lieberman M A, Lichtenberg A J and Kawamura E 2008 *Phys. Rev. Lett.* **101** 085004
[68] Ellmer K, Wendt R and Wiesemann K 2003 *Int. J. Mass Spectrometry* **223-4** 679–93
[69] Han D M, Liu X Y, Xu J and Wang Y N 2018 *Chinese Phys.* B **27** 065202
[70] Wen D Q, Krek J, Gudmundsson J T, Kawamura E, Lieberman M A and Verboncoeur J P 2021 *Plasma Sources Sci. Technol.* **30** 105009